Spatial evolution of the electron-energy distribution in the vicinity of a discharge-tube constriction

V. Godyak, R. Lagushenko, and J. Maya

GTE Electrical Products, Danvers, Massachusetts 01923

We report experimental and calculational results of the spatial evolution of the electron-energy distribution function (EEDF) mean electron energy $\bar{u}$, electric field E, and plasma density N_e, in the vicinity of a sharp constriction in a low-pressure mercury–rare-gas discharge. We explain many of the features of the EEDF by noting the absence of equilibrium between the electrons and the electric field. Our one-dimensional model of the spatial evolution of the EEDF is in good agreement with experimental results.

I. INTRODUCTION

Sudden changes in the electric field E of steady-state electrical discharges are of intrinsic interest both from the fundamental as well as the applied points of view. An understanding of such phenomena may lead to the control and exploitation of such changes for technological applications.[1]

A practical way to obtain sudden changes of the electric field is to use a sharp constriction of the discharge tubes. The discharge which we describe in this paper is a low-pressure collision-controlled discharge in the Hg–rare-gas mixture, with a sharp constriction in the form of an orifice [Fig. 1(a)].

Discharges with sharp changes in the diameter of the tube [Fig. 1(b)] have been used over the years to study the "double-layer" phenomenon. Double layers are essentially the transition regions in a plasma composed of two adjacent layers with opposite sign of the space charge.

Existence of a double layer in collisionless plasmas is typically accompanied by such phenomena as trapped particles, plasma-wave instabilities, and wave-particle interaction. A great deal of work on double layers has been done for collisionless plasmas with a single species, with the emphasis on the aforementioned phenomena.[2–6]

(a)

(b)

FIG. 1. Different kinds of discharge-tube constrictions.

Since the discharge we studied has a constriction, it has formal similarity to constricted discharges used to generate double layers. However, significant differences exist. The discharge we studied is a collision-controlled discharge in a mixture of mercury and a rare gas. This discharge forms the basis of a fluorescent lamp and the main energy-loss mechanism is radiation. Typically in our experiments, the orifice diameter d_o is on the order of 1 cm and the full length of the transition region near the orifice is close to 3–4 cm. For the same conditions, the Debye length is $\lambda_D \simeq 10^{-2}$ cm and the electron mean free path is $\lambda_e \simeq 0.1$ cm (at $P_{Ne} = 1$ torr). These numbers show that the plasma in the vicinity of the orifice has to be quasineutral and collision controlled. Furthermore, the electron-velocity distribution function is expected to be close to spherically symmetric in velocity space. But the gas pressure is not too high and so the electron-energy relaxation length λ_ε is not much less than the scale of the phenomenon. Thus the electrons are not in equilibrium with the electric field. Since the discharge is collision controlled, the specific plasma-wave phenomena of double layers are suppressed. Therefore we believe the transition region near the constriction may or may not have the characteristics of a double layer, but this will have no significant influence on the mechanism of the discharge. We believe that the key to understanding the constriction mechanism is that the constriction results in the development of a sharp electron-accelerating potential drop. This leads to significant changes of the electron-energy distribution function (EEDF) and the energy and ionization balances of the plasma compared to conditions in a straight tube. These topics will be discussed further.

We have studied, both experimentally and by calculations, the EEDF, the potential distribution, and other plasma parameters in the vicinity of the orifice. Preliminary results of this study have been reported in Refs. 7 and 8.

Probe measurements of the EEDF have also been done by Anderson at the tube constriction [Fig. 1(b)] in the

low-pressure mercury discharge.[6] Existence of a strong electric field in the vicinity of a constriction [Fig. 1(b)] in the collisional discharge in helium has been recently studied by Ganguly and Garscadden[9] using Stark spectroscopy.

While discharges with sharp changes in diameter of the tube [Fig. 1(b)] have been studied over the years,[2-6] we are not aware of publications in which the discharge has a sharp constriction both from the anode as well as cathode side [Fig. 1(a)], much like a thin aperture used in optics. In Secs. II and III we describe our probe measurements of the EEDF and other parameters of the plasma. In Sec. III we describe our experimental observations, their interpretation and implications, and our initial attempts to model this discharge. Mathematical details of our simplified discharge model are given in the Appendix.

II. EXPERIMENTAL TECHNIQUE

We have measured the axial distribution of the plasma parameters in the vicinity of the orifice of the partitioned discharge using Langmuir probes. In our experiments the energy spectrum of the electrons could differ considerably from a Maxwellian one. This makes the concept of electron temperature not valid and the traditional Langmuir technique not applicable to obtain plasma parameters. We obtained plasma parameters such as plasma density N_e and mean electron energy $\bar{u}$ from experimental data of the electron-energy distribution function by calculating integrals of the EEDF as follows:

$$N_e = \int_0^\infty F(u)du, \quad \bar{u} = \frac{1}{N_e} \int_0^\infty uF(u)du .$$

Here $F(u)$ is the EEDF.

The EEDF was found from absolute measurement of the second derivative of the probe current by the probe voltage, d^2I_p/dV^2, using the Druyvesteyn formula,

$$F(u) = \frac{2}{e^2S} \left[\frac{2mV}{e} \right]^{1/2} \frac{d^2I_p}{d^2V}, \quad eV = u .$$

Here S is the probe surface area and V is the probe sheath voltage. The conventional way of obtaining the second derivative is by electronic differentiation.[10] This is typically done by applying a small rf voltage to the probe and measuring some of the components of the probe current which are proportional to its second derivative. Depending on the kind of applied rf voltage, this component of the probe current could be measured as a second harmonic, an envelope, or a beat frequency signal.[10] In all these cases, averaging with a lock-in amplifier with relatively slow scanning of the probe voltage is used. A serious problem with the slow probe-voltage scanning is a change in the probe work function during the sweep time due to probe heating by the probe current.[11] Fast pulse scanning of the probe voltage for a time short enough to maintain the probe temperature constant during the measurement enables one to eliminate the effects of change in the probe work function.[12] However, using a fast sweep of the probe voltage for a time less than, say, 1 ms, makes

it impossible to use lock-in amplifier techniques, since that requires a considerable time for averaging. Another way to obtain a second derivative of the probe current is by differentiation of the probe current in the time domain. In this case, for a probe voltage scanning linearly in time, the second derivative of the probe current with respect to time is proportional to the second derivative of the probe current with respect to voltage. This method has been used for EEDF measurements in high-density plasmas where the frequency of the scanning voltage has been chosen to be far greater than that of the plasma noise spectra.[13] Unfortunately, this method can be applied for quiescent plasmas only. For the measurement of the second derivative in the noisy neon-mercury discharge we used a plasma-noise-suppression circuit with a second reference probe. This, in combination with fast pulse measurement ($\tau_m = 0.5$ ms), enabled us to obtain a nondistorted EEDF with high resolution and dynamic range.[14] The idea of noise suppression is to introduce a noise signal of opposite phase into the probe measurement circuit.[15]

In our experiment [see Fig. 2] we used a reference probe P_1 which was placed in the same plane with a measurement probe P_2. The noise voltage, reference ground, was picked up by the reference probe and was introduced in an opposite phase to the cathode of the discharge by means of a high-voltage high-frequency operational amplifier OP_2 (Apex Microtechnology Corp. PA84). The same operational amplifier worked as the driver of the scanning voltage. The latter was introduced into the positive input of OP_2 by the 10-gain preamplifier OP_1 (PA84). The OP_2 produced an output voltage which, when applied to the cathode, made the plasma potential in the vicinity of the probe equal to the input voltage of OP_2 on its positive input minus a floating potential difference of the reference probe P_1. In the case when scanning voltage was equal to zero, the OP_2 automatically kept the measurement probe P_2 floating (probe current equal to zero). The appearance of any noise or dc voltages between the cathode and the plasma potential near
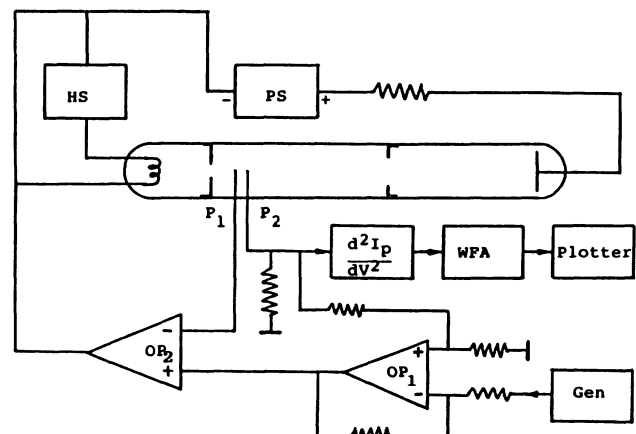

FIG. 2. Experimental setup for plasma probe measurements. PS is the power supply and HS is the heater supply.

the probes has been compensated for in the measurement probe circuit due to deep negative feedback. The measurement of the probe current-voltage characteristic (actually current-time characteristic) was performed as follows. A triangle waveform voltage from the Wavetek 193 generator was applied to the cathode of the discharge through the OP_1 and OP_2 amplifiers. This caused the discharge as a whole to sweep at 20 V/MS with respect to ground, which in turn provided a probe current flow through the grounded sensitive resistor R. The probe current signal generated on the resistor R was fed into the analogue filter-differentiator which generated the instantaneous value of the second derivative. The cutoff frequency of the filter differentiator was 20 kHz. The second-derivative signal d^2I_p/dt^2 was further applied to the waveform analyzer (WFA) (Analogic, Data 6000) working in compressed 12-bit analog-to-digital conversion mode to perform the averaging. The averaged signal of the second derivative was fed into the VAX 780 computer which calculated the EEDF and its integrals: plasma density N_e and mean electron energy $\bar{u}$. The absolute plasma-potential values were measured by monitoring oscillograms of the second derivative and the scanning voltage. The plasma potential was found as the scanning-voltage value corresponding to zero crossing at the second-derivative oscillogram, taking into account the time delay of the filter differentiator.

The plasma probe measurements were performed in a discharge tube of 5.0 cm diameter having 1 torr Ne and mercury vapor corresponding to 20 and 40 °C. The mercury pressure was controlled by the cold-spot temperature, while the entire discharge tube was maintained at a slightly higher temperature. The two tungsten probes of 3 mm length and 0.05 mm of radius were placed in the middle of the discharge tube close to its axis. Two movable metal diaphragms with different orifice diameters $d_o = 1.25$ and 2.5 cm were placed on both sides of the probes. By changing the position of one diaphragm and keeping the other far away from the probes we could make measurements for different distances between probe and orifice plane. Having cathodes on both ends of the tube we could obtain results for both sides of the diaphragm, by changing the direction of the discharge current.

III. EXPERIMENTAL RESULTS, MODELING, AND DISCUSSION

The axial distributions of the plasma potential V, the electron number density N_e, and the mean electron energy $\bar{u}$ are shown in Figs. 3–5 for orifice diameters 1.25 and 2.5 cm. A smaller orifice diameter results in a much greater perturbation of the plasma parameters. As one can see, the value of the axial electric field $|E| = dV/dx$, and N_e and $\bar{u}$ reach their maximums close to the orifice. The maximum value of E at the orifice is five times higher than in the undistorted positive column in the case of orifice diameter $d_o = 1.25$ cm. Existence of a sharp electron-accelerating voltage drop is clearly visible on the cathode side of the orifice for this case. This can be expected for the following reasons.

Since the current density at the orifice has to be higher, an increase of the electron number density and drift velocity is required. To achieve this, the discharge develops a strong electric field near the orifice. The strong electric field increases the drift velocity and maintains a higher plasma density by compressing the plasma and providing an increase in the ionization. However, the increase of plasma density is only about 3 times versus 16 times of the current density. Apparently, this is due to a great increase of the drift velocity. On the anode side, the plasma gradually relaxes to the undistorted conditions of the positive column. Note nonmonotonic behavior of the plasma parameters in the transition region.

The electric field changes sign twice before it gets back to the undistorted positive-column value. One can observe the region of the electron-decelerating electric field on the anode side. This can be explained as follows. The field in the vicinity of the orifice is the sum of two components: the resistive component E_r and the ambipolar diffusion component E_a. The total field and the components E_r and E_a can be represented as follows:

$$E_t = E_a + E_r, \quad E_r = J/\sigma, \quad E_a = -c\nabla(\bar{u}N_e)/eN_e,$$

where J, σ, and c are the current density, the plasma conductivity, and a numerical coefficient, respectively. The ambipolar component has the opposite sign to the resistive one and prevails on the anode side.

This situation is typical for conditions when the electron diffusion current is greater than the total current. The behavior of the plasma parameters in the transition region on the anode side of the orifice bears a great
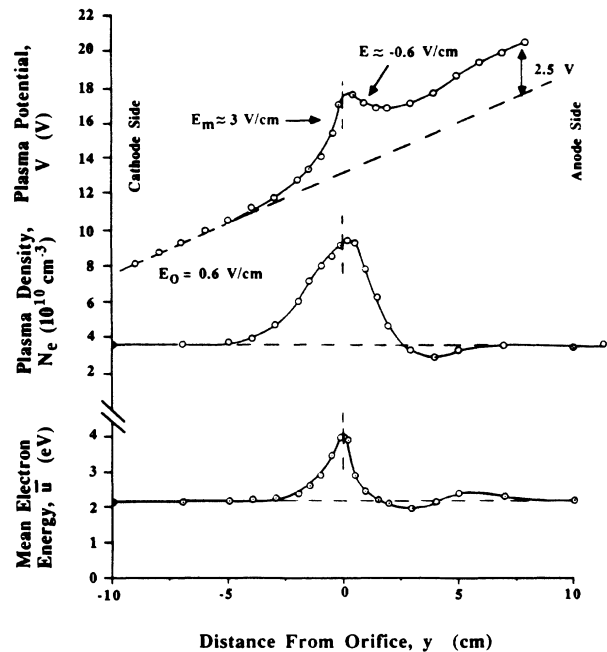

Distance From Orifice, y (cm)

FIG. 3. Distributions of plasma parameters as a function of distance from the orifice y. Here $P_{Ne} = 1$ torr, cold-spot temperature of Hg $T_c = 40$ °C, discharge diameter $D = 5.0$ cm, orifice diameter $d_o = 1.25$ cm, discharge current $I = 0.2$ A.
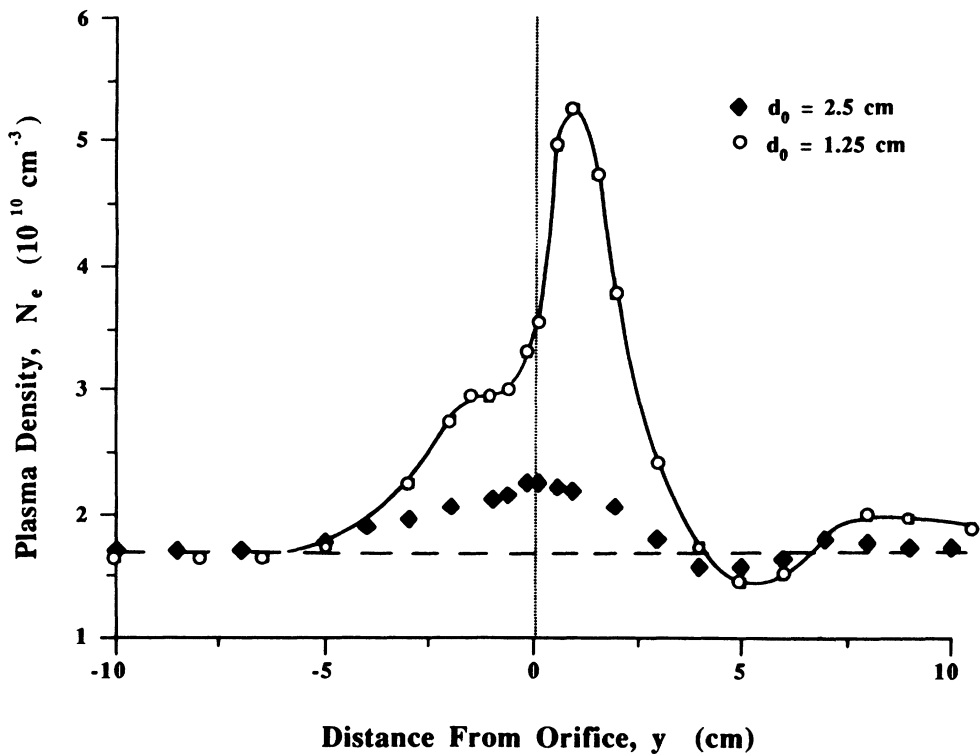
FIG. 4. Plasma density for two different orifice diameters d_o. Here $P_{Ne} = 1$ torr, $D = 5.0$ cm, $T_c = 20\,°C$, $I = 0.1$ A.
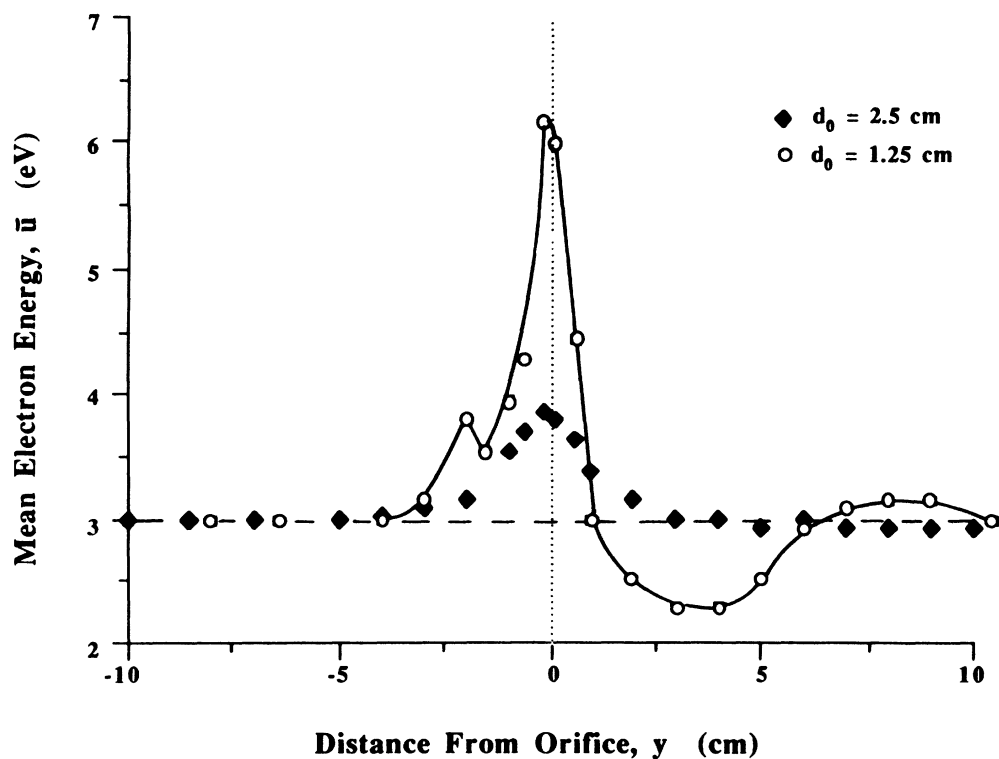

FIG. 5. Mean electron energy $\bar{u}$ for two different orifice diameters as a function of distance from the orifice y. Here $P_{Ne} = 1$ torr, $D = 5.0$ cm, $T_c = 20\,°C$, $I = 0.1$ A.

resemblance to the negative glow region in the vicinity of the cathode.[16] This is due to the similarity in the physical phenomena in both cases.

Note, the EEDF at the orifice is greatly enriched by fast electrons compared to the undistorted positive-column conditions. This can be seen from our experimental results of the EEDF shown in Figs. 6 and 7. Apparently, this enables the discharge to maintain ionization balance without further acceleration of electrons. Such a situation is analogous to the negative glow where ionization is produced by electrons accelerated by the cathode voltage drop.

The evolution of the EEDF measured along the axis on both sides of the orifice is shown in Figs. 6 and 7. One can observe the gradual shift of the EEDF upwards along the energy scale when approaching the orifice from the cathode side. The shift is accompanied by the appearance of the group of slow electrons. These tendencies are especially clear in the case of lower mercury pressure (Fig. 7). Here, one can observe the EEDF with two distinct maxima. The opposite process of the EEDF relaxation takes place on the anode side of the orifice. In the case of lower mercury pressure one can see the second region of electron acceleration followed by relaxation.

Note the absence of the direct correlation between the electric field and the mean electron energy. The mean electron energy remains comparable to its maximum value even at the points where $E = 0$. This, as well as many observed features of the EEDF, can be explained

by effects of nonequilibrium between electrons and the electric field. Nonequilibrium can be expected at our conditions.

The dominant mechanism of the electron energy loss at our conditions appears to be the inelastic collisions with mercury atoms. The energy relaxation length in that case can be estimated as

$$\lambda_\varepsilon = 1/(3NN_{Hg}q_t q^*)^{1/2} .$$

Here N, N_{Hg} are the number densities of the rare gas and mercury, and q_t, q^* the momentum-transfer cross section and inelastic cross section of mercury, respectively.

For typical conditions $P = 1$ torr, $P_{Hg} = 6$ μm, the energy relaxation length is about $\lambda_\varepsilon = 1.5$ cm. This is about equal to the length of the potential-drop region defined as d (see Fig. 8). Note, also, electrons with energy less than the first excitation potential $u_1 \simeq 5$ V, can travel without loss of energy until they are accelerated up to energy $u = u_1$. This effectively increases the length of the energy relaxation. Thus there can be a significant nonequilibrium. At nonequilibrium conditions, in an accelerating field, the EEDF at the point y can be qualitatively visualized as composed of two electron groups. The higher-energy group corresponds to the initial electrons at $y = -d$, which arrive to the point y without an energy loss. If $F_0(y)$ is the EEDF at $y = -d$, then the contribution of these electrons can be described as the energy-shifted distribution $F_0(u + (y + d)E)$. The lower-energy
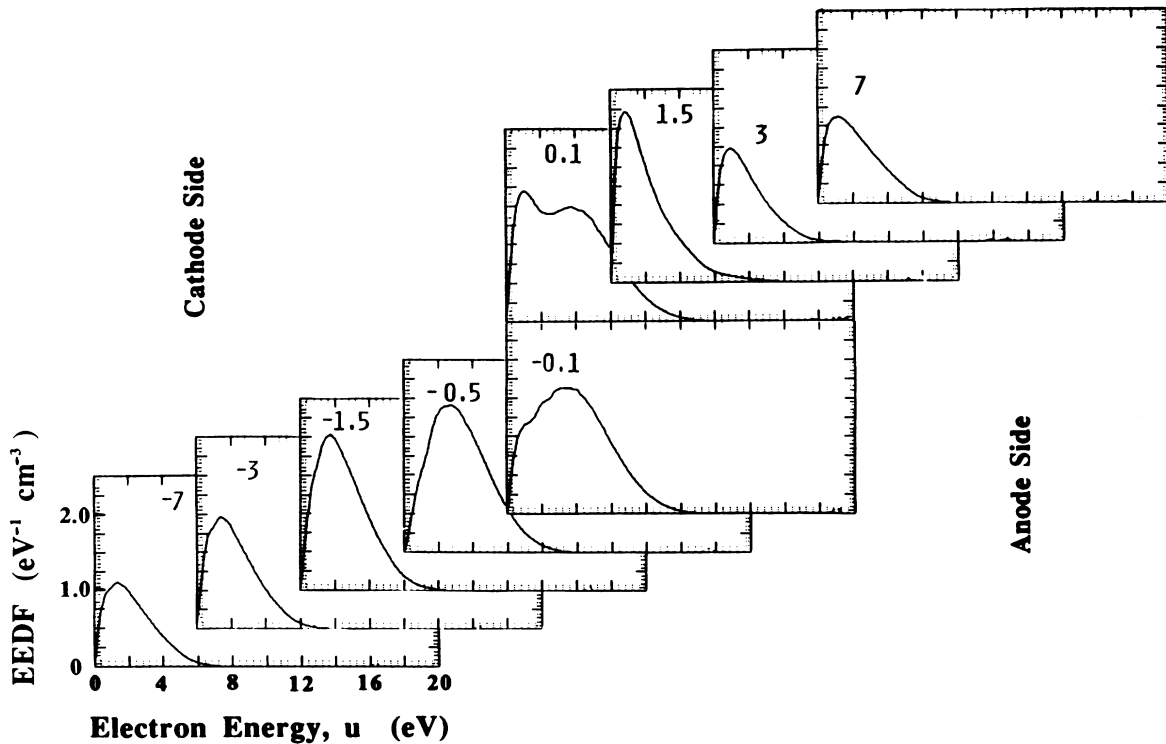

FIG. 6. Spatial evolution of the EEDF along the discharge (the numbers inside each rectangular box indicate the distance in centimeters from the orifice). Here $P_{Ne} = 1$ torr, $T_c = 40$ °C, $D = 5.0$ cm, $d_o = 1.25$ cm, $I = 0.2$ A. The EEDF is expressed in units of 10^{10} eV^{-1} cm^3.
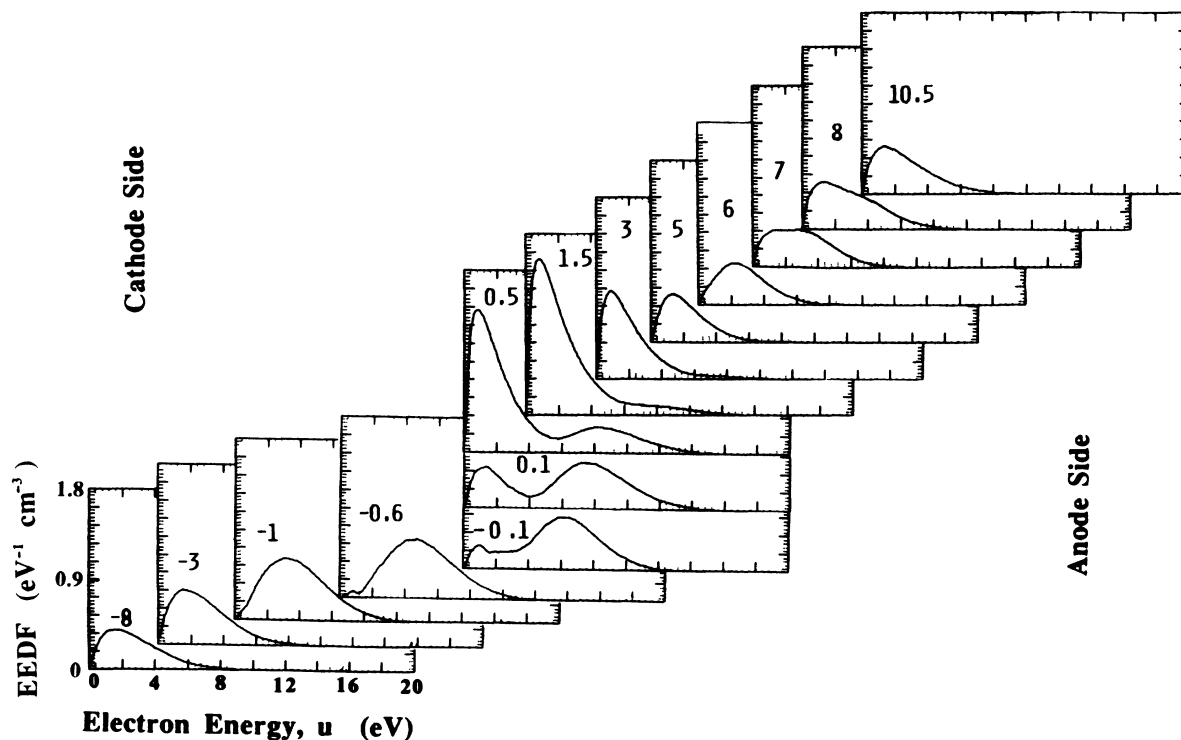
FIG. 7. Spatial evolution of the EEDF along the discharge (the numbers inside each rectangular box denote the distance from the orifice in centimeters. Here $P_{Ne} = 1$ torr, $T_c = 20\,°C$, $D = 5.0$ cm, $d_o = 1.25$ cm, $I = 0.1$ A. The EEDF is expressed in units of 10^{10} $eV^{-1} cm^3$.

group appears as a result of energy losses on the way to the point y. This picture appears to be in qualitative agreement with the experimental data of the EEDF on the cathode side of the orifice. To account for a fast relaxation of the EEDF in the region of the weak electron-decelerating field on the anode side, one has to consider both effects of collisions and energy-dependent electron diffusion.

The effect of the downward energy shift is also possible. However, the total decelerating potential drop is close to $\Delta V \simeq -0.5$ V, whereas the mean electron energy at the orifice is close to $\bar{u} \simeq 4$ eV. Therefore the downward shift is probably not very important.

The concept of the energy-shifted distribution has been used by Anderson[6] to interpret his probe data of the EEDF at the tube constriction of the shape shown in Fig. 1(b). However, the treatment used by Anderson is applicable quantitatively only at collisionless conditions. Numerical calculations of the EEDF without a prior assumption of the electron-field equilibrium have been performed in Refs. 17–23. However, these results cannot be directly applied to our case due to differences in the gas medium, electric field shape, etc. The situation studied by Moratz, Pitchford, and Bardsley[23] bears the closest resemblance to our case. The shape of increasing electric field considered in this work is qualitatively close to the shape in our work on the cathode side of the orifice. The qualitative behavior of the EEDF and mean electron energy observed in Ref. 23 appear to be close to our observations. Nevertheless, these results cannot be directly

compared to our results, since they were obtained for nitrogen and much greater values of E/N. Therefore we have developed a simplified theoretical model which permits us to obtain an analytical expression of the EEDF for our nonequilibrium conditions. Basic assumptions of the model were as follows.
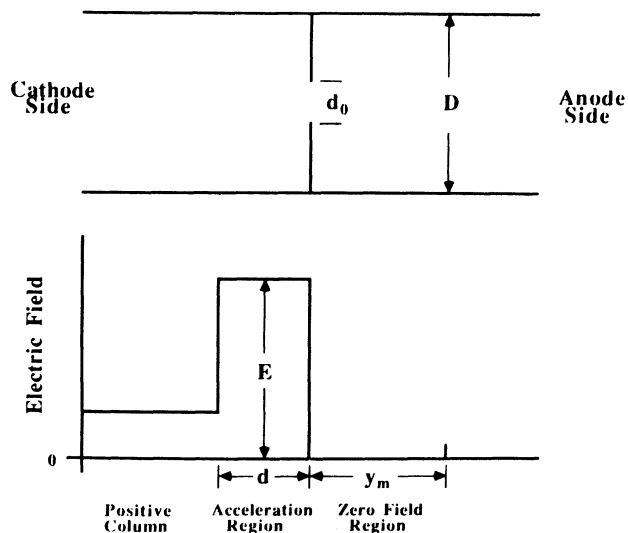

FIG. 8. Simplified one-dimensional profile of the electric field in the vicinity of the orifice. This is the profile used in the calculations. (See text for definition of y_m.)

V. GODYAK, R. LAGUSHENKO, AND J. MAYA

We have used a simplified one-dimensional profile of the electric field. The following two spatial regions have been considered in the vicinity of the orifice. This is shown in Fig. 8.

(1) The region of the potential drop in front of the orifice on the cathode side. The electric field in this region has been approximated by the constant value E. The value of E and the length of this region d have been taken from the experimental data.

(2) The region on the anode side of the orifice, up to the point where the electric field begins to rise again. The length of this region has been denoted as y_m. In this region, we have neglected a relatively small variation of the potential and treated this region as a quasiequipotential one, setting $E = 0$.

We have assumed the only mechanism of energy loss to be inelastic collisions with mercury atoms and neglected the influence of the generation of new electrons on the shape of the EEDF. For simplicity's sake, we have considered only one value of the inelastic energy loss $u_1 = 5$ eV. This value is very close to the average value of the excitation potential for the first excited states of mercury $6\,^3P_{0,1,2}$ and $6\,^1P$.

The electron-velocity distribution function $f(\mathbf{v},x)$ has been represented in the usual approximate form,

$$f(\mathbf{v},x) = f_0(v,x) + \frac{v_x}{v} f_1(v,x) \ .$$

Here v is the electron velocity and x is the spatial coordinate. $x = 0$ corresponds to the beginning of the electron-accelerating voltage drop on the cathode side of the orifice; notice that $x = y + d$. The EEDF can be expressed as

$$F(u,x) = \sqrt{u}\, f_0(u,x) \ .$$

The functions f_0 and f_1 satisfy the system of equations which follows from the Boltzmann equation and is well described in the literature.

Using the assumptions of our model, one can solve these equations analytically and derive the expressions for f_0 and f_1 applicable to nonequilibrium conditions. The equations, their mathematical treatment, and the expressions for f_0 and f_1 are described in detail in the Appendix. Here we proceed to the discussion of the results and their comparison to the experimental data.

For the case of mercury at a pressure $P_{Hg} = 6$ μm (the cold-spot temperature $T_c = 40\,°(C)$, calculations have been performed with $d = 1.25$ cm, $Y_m = 1.5$ cm, the undistorted positive-column field $E_0 = 0.6$ V/cm, and the potential-drop field $E = 2.8$ V/cm.

Since measurement of the potential has not been done for mercury pressure $P_{Hg} = 1.2$ μm (the cold-spot temperature $T_c = 20\,°(C)$, the estimated values $E = 3$ V/cm, and $d = 1.25$ cm have been used. The value of E_0 has been calculated with our model of the positive column to be equal to $E_0 = 0.7$ V/cm. Calculated values of the mean electron energy for $P_{Hg} = 6\,\mu$m are shown in Fig. 9.

Note that the mean energy as well as other parameters calculated with our model are discontinuous at the position of the orifice. This discontinuity is due to the
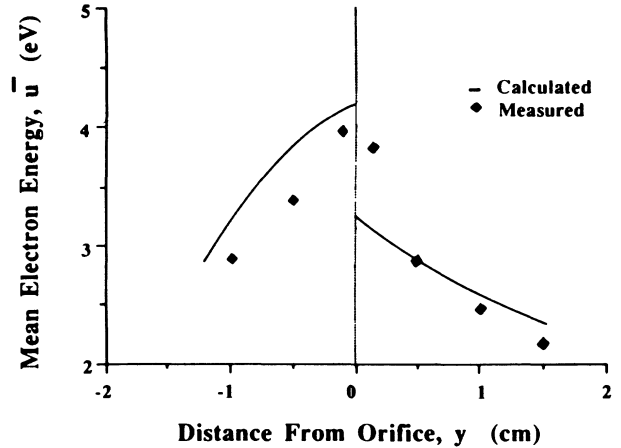

FIG. 9. Calculated and measured mean electron energy u as a function of distance from the orifice y. Here $d_o = 1.25$ cm, $T_c = 40\,°C, I = 0.2$ A.

discontinuous approximation of the electric field. However, this discontinuity appears to be a reasonable approximation to reality, since experimental values decrease sharply beyond the orifice. Calculated and experimental mean energies agree within 10%. This agreement is beyond expectations, since our model does not take into account effects of the radial compression and expansion of the plasma in the vicinity of the orifice.

The nonequilibrium effects can be demonstrated by calculating the inelastic collision coefficient

$$\alpha^*(x) = \left[\frac{2e}{m} \right]^{1/2} N_{Hg} \int_{u_1}^{\infty} \frac{u q^*(u)}{J} f_0 \, du \ ,$$

where J is the current density. The value of α^* gives the average number of inelastic collisions per unit length. The value $P(x)$,

$$P(x) = \exp \left[- \int_0^x \alpha^*(z) dz \right] \ ,$$

gives the probability for electrons to travel a distance x without undergoing any inelastic collisions. Calculated values of α^* are given in Fig. 10 for the case $P_{Hg} = 6$ μm.

The area S_d underneath the curve $\alpha^*(x)$ between $x = 0$ and d gives the number of inelastic collisions which an electron undergoes when passing through the potential-drop region. In our case, for $P_{Hg} = 6$ μm, this is equal to $S_d = 0.33$. Since the ratio $u_1 S_d / Ed = 0.49$, then about 50% of the energy which an electron gains in the region of potential drop is carried forward to the quasiequipotential region. This signifies a considerable deviation from the electron-field equilibrium. Note, this implies that the regions of energy gain and energy loss are separated in space. This feature is a substantial deviation from the conventional positive-column discharge where energy deposition and energy dissipation always go hand in hand.

The total number of inelastic collisions per electron from the beginning of the potential drop to the end of the quasiequipotential region is equal to $S_t = 0.69$. Note, the
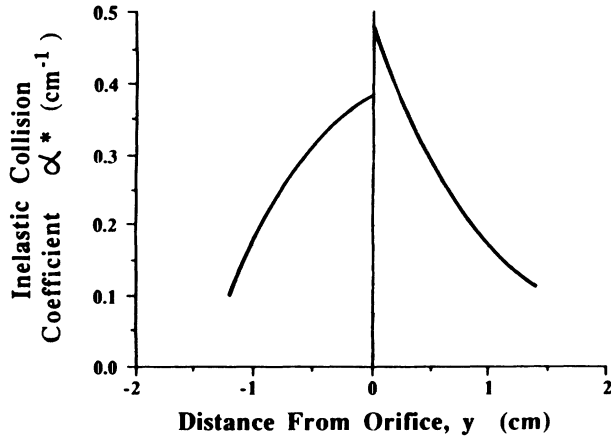
FIG. 10. Calculated inelastic collision coefficient, α^*, as a function of distance from the orifice y. Here $d_o = 1.25$ cm, $T_c = 40\,°C$.

ionization cross section is included in the inelastic cross section q^*, so the value S_t includes the contribution of the direct ionization. However, since the ionization potential of mercury $u_i = 10.4$ V and $f_0(u_i,x) \ll f_0(u_1,x)$, then the number of direct ionizations is $S_i \ll S_t < 1$.

The two-step ionization via mercury metastables is probably more important. The number of two-step ionizations can be estimated as

$$S_i^* \simeq \frac{N_m}{N_{Hg}} S_t ,$$

where N_m is the metastable number density. Since the ratio N_m/N_{Hg} is expected to be much less than unity, then $S_i^* \ll 1$. Thus, the number of new electrons generated per one electron is expected to be much less than unity. This justifies our neglect of the appearance of new electrons in the kinetic equation. Calculated and experimental values of the EEDF normalized to the equal areas are compared in Figs. 11–13, $P_{Hg} = 6$ and $1.2\ \mu m$.

The calculated EEDF on the cathode side of the orifice shows the same tendency to be shifted upward as the electrons approach the orifice. However, this tendency appears to be exaggerated as compared to experiment. Also, the distinction between the higher- and lower-energy electron groups is less prominent for the experimental EEDF than for the calculational one. We believe these differences are due to the three-dimensional structure of the potential drop and the plasma compression effects not taken into account in our theoretical model. An interesting phenomenon is the rapid change of the experimental EEDF shape within the distance 0.1–0.2 cm on the anode side of the orifice. Note that this distance is significantly shorter than the distance of the energy relaxation due to inelastic collisions, λ_ϵ. We believe that this phenomenon is due to a rapid decrease of the electric field combined with a much slower diffusion of lower-energy electrons. Since electrons pumped in from the cathode side have to be taken away by diffusion, this results in the accumulation of lower-energy electrons on
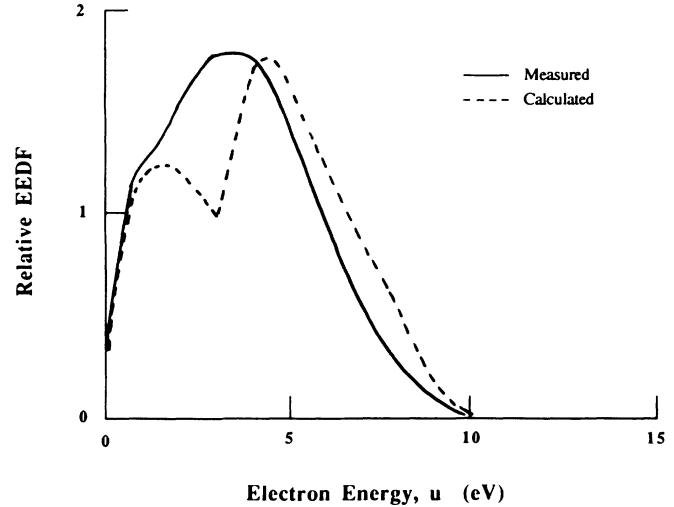

Electron Energy, u (eV)

FIG. 11. Calculated and measured relative EEDF for $y = -0.1$ cm (i.e., on the cathode side of the orifice). Here $d_o = 1.25$ cm, $T_c = 40\,°C$, $P_{Ne} = 1$ torr.

the anode side. The effect can be further amplified by the existence of the electron-decelerating field on the anode side.

The rapid change of the EEDF on the anode side is simulated qualitatively by our model. The quantitative differences can be ascribed to the plasma expansion on the anode side and the smoothing effect of the electron-electron interaction. Note, although the electron-electron interaction appears to be weak in general for our conditions, its effect can be greatly amplified when the EEDF varies rapidly, since the electron-electron interaction depends on the magnitude of the derivatives of the EEDF with respect to energy.
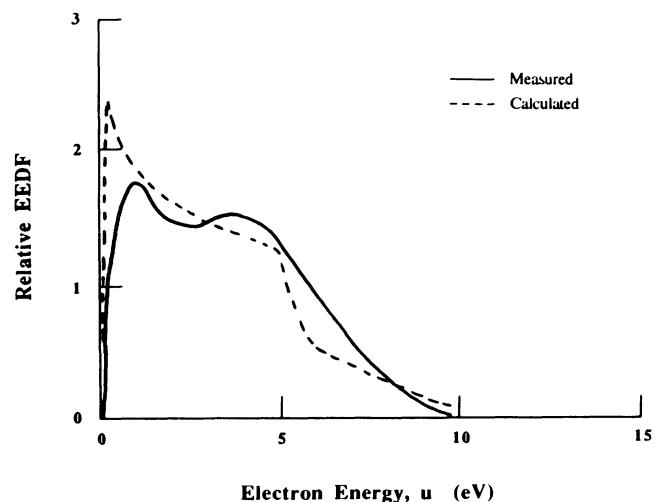

Electron Energy, u (eV)

FIG. 12. Calculated and measured relative EEDF for $y = 0.1$ cm (i.e., on the anode side of the orifice). Here $d_o = 1.25$ cm, $T_c = 40\,°C$, $P_{Ne} = 1$ torr.
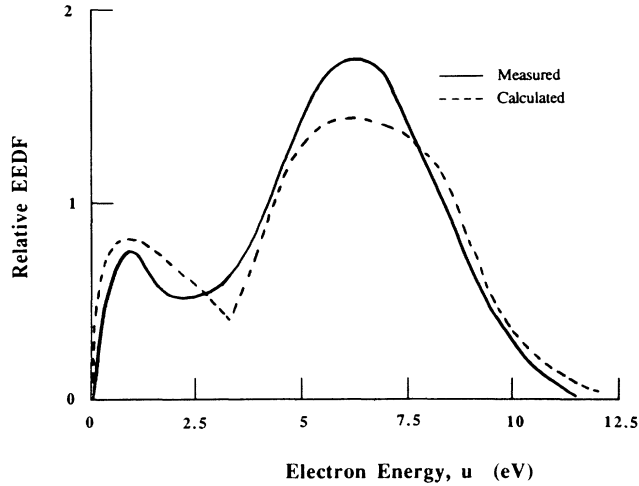
FIG. 13. Calculated and measured EEDF for $y = -0.1$ cm (on the cathode side). Here $d_o = 1.25$ cm, $T_c = 20\,°C$, $P_{Ne} = 1$ torr.

In summary, we report studies of plasma parameters in a collisional low-pressure Hg–rare-gas discharge where the EEDF and E are not in equilibrium. The basic features of the EEDF observed in our experiments can be correlated with the shape of the electric field if the electron-field nonequilibrium effects are taken into account.

We have demonstrated that this phenomenon offers a simple way of controlling the EEDF. Furthermore, we demonstrate that this sharp constriction offers a convenient way of separating the energy input and energy dissipation mechanisms in the discharge. We have studied discharge parameters such as plasma density, electric field, electron mean energy, and EEDF, as well as their spatial evolution.

Our simplified theoretical model accounts for many observed features of the EEDF qualitatively. A more quantitative agreement can be expected if a realistic three-dimensional geometry and the electron-electron interaction are taken into account. However, this appears to represent a formidable numerical task.

ACKNOWLEDGMENT

APPENDIX

We use in the following all the assumptions of our simplified one-dimensional model described in Sec. III.

If the electron-velocity distribution function $f(\mathbf{v}, x)$ is represented in the usual form

$$f(\mathbf{v}, x) = f_0(v, x) + \frac{v_x}{v} f_1(v, x) , \tag{A1}$$

then equations for f_0 and f_1 obtain the form

$$\frac{\partial}{\partial x}\left[\frac{uf_1}{3N}\right] + \frac{\partial}{\partial u}\left[\frac{Euf_1}{3N}\right]$$
$$= [(u + u_1)q^*(u + u_1)f_0(u + u_1)$$
$$- uq^*(u)f_0(u)]N_{Hg} , \tag{A2}$$

$$\frac{\partial f_0}{\partial x} + E\frac{\partial f_0}{\partial u} = -Nq_t f_1 .$$

The function f_0 has been normalized as

$$\int_0^\infty \sqrt{u}\, f_0\, du = N_e(x) ,$$

where $N_e(x)$ is the electron number density. Here q^* is the total inelastic cross section of mercury; q_t is the momentum-transfer cross section; N, N_{Hg} are the total and mercury atom number density, respectively; E is the electric field intensity; and $u = mv^2/2e$ is the electron kinetic energy in volts.

1. The region in front of the orifice

We introduce new variables

$$w = u, \quad \varepsilon = u - Ex . \tag{A3}$$

The variable ε is the sum of kinetic and potential energies of the electron. The variable w is equal numerically to the kinetic energy, but any derivatives or integrals with respect to w will mean that the operation is conducted at the fixed value of ε. With variables (A3), the system (A2) can be rewritten as

$$\frac{\partial}{\partial w}\left[\frac{w}{q_t}\frac{\partial f_0}{\partial w}\right]$$
$$= \frac{3NN_{Hg}}{E^2}[(w + u_1)q^*(w + u_1)f_0(w + u_1, \varepsilon + u_1)$$
$$- wq^*(w)f_0(w, \varepsilon)] ,$$

$$f_1 = -\frac{E}{Nq_t}\frac{\partial f_0}{\partial w} . \tag{A4}$$

The inelastic cross section of mercury is equal to zero for $u < 4.7$ V, so one can approximate the function $q^*(w)$ as $q^* = 0$ for $w < u_1 = 5$ V. We consider further the following two energy domains.

(i) $w < u_1$.

(ii) $w \geq u_1$.

We restrict ourselves to conditions when

$$f_0(u + u_1, x) \ll f_0(u, x) . \tag{A5}$$

Accepting condition (A5), we are restricted to not too large values of the parameters $E^2/3NN_{Hg}$ and Ed. The requirement (A5) is well satisfied at the conditions of our experiments. Note that the above restriction on the value of E does not imply that electrons are close to equilibrium with the electric field.

Thus, neglecting the small term proportional to $f_0(w + u_1, \varepsilon + u_1)$, Eq. (A4) can be reduced to

$$\frac{\partial}{\partial w}\left[\frac{w}{q_t}\frac{\partial f_0}{\partial w}\right]-\frac{3NN_{Hg}}{E^2}wq^*(w)f_0(w)=0 \ . \qquad (A6)$$

The required solution of Eq. (A6) can be represented in the form

$$f_0(w,\varepsilon)=C_2(\varepsilon)\phi(w) \ , \qquad (A7)$$

where $C_2(\varepsilon)$ is an arbitrary function of the full energy. The function $\phi(w)$ is a particular solution of Eq. (A6) satisfying the following conditions: $\phi(w)\to0$ if $w\to\infty$ and $\phi(u_1)=1$.

In the domain (i), one can obtain from Eqs. (A4) and (A7) the following expression for $f_0(w,\varepsilon)$:

$$f_0(w,\varepsilon)=C_0(\varepsilon)-C_1(\varepsilon)\int_w^{u_1}\frac{q_t(w)}{w}dw$$
$$+C_2(\varepsilon+u_1)\int_w^{u_1}I(w+u_1)\frac{q_t(w)}{w}dw \ . \qquad (A8)$$

Here $C_0(\varepsilon)$ and $C_1(\varepsilon)$ are arbitrary functions of the full energy, and the functions $I(w)$ is defined as

$$I(w)=\frac{3NN_{Hg}}{E^2}\int_{u_1}^w wq^*(w)\phi(w)dw \ . \qquad (A9)$$

Note a useful formula, as will be clearer later on, resulting from Eq. (A6), is

$$\frac{w}{q_t(w)}\phi'(w)-\frac{u_1}{q_t(u_1)}\phi'(u_1)=I(w) \ . \qquad (A10)$$

The formulas (A7)–(A9) give the general form of the function $f_0(w,x)$, depending on the choice of the functions $C_0(\varepsilon),C_1(\varepsilon),C_2(\varepsilon)$. The case $C_1(\varepsilon)=0$, $C_0=C_2=$const corresponds to the spatially uniform solution when electrons are in equilibrium with the electric field.

In our case the functions C_0,C_1,C_2 are determined by the boundary condition at $x=0$, the condition of continuity of f_0 with respect to variables u and x, and by the condition of the electron flux conservation. The condition of continuity requires $C_0(\varepsilon)=C_2(\varepsilon)$. The electron flux density for the function f_0 given by Eqs. (A7) and (A8) is equal to

$$j=-\frac{1}{3}\left[\frac{2e}{m}\right]^{1/2}\frac{E}{N}\left[\int_0^{u_1}C_1(\varepsilon)du\right.$$
$$-\int_0^{u_1}C_2(\varepsilon+u_1)I(u+u_1)du$$
$$\left.+\int_{u_1}^\infty\frac{u}{q_t}\phi'(u)C_2(\varepsilon)du\right] \ . \qquad (A11)$$

For reasons that will be clearer later, we represent the function $C_2(\varepsilon)$ as

$$C_2(\varepsilon)=\Phi(\varepsilon)+B_2 \ , \qquad (A12)$$

where $\Phi(\varepsilon)$ is a function of ε and B_2 is a constant. Using Eqs. (A5), (A10), and (A12), the formula (A11) can be reduced to the formula

$$j=-\frac{1}{3}\left[\frac{2e}{m}\right]^{1/2}\frac{E}{N}\left[B_2\frac{u_1^2\phi'(u_1)}{q_t(u_1)}+\int_0^{u_1}C_1(\varepsilon)du\right.$$
$$\left.+\frac{u_1\phi'(u_1)}{q_t(u_1)}\int_{u_1}^{2u_1}\Phi(\varepsilon)du\right] \ . \qquad (A13)$$

The analysis of the formula (A13) shows the flux does not depend on the coordinate x if

$$C_1(\varepsilon)=\frac{u_1\phi'(u_1)}{q_t(u_1)}\Phi(\varepsilon) \ , \qquad (A14)$$

and the function $\Phi(\varepsilon)$ is continued periodically in the region of $\varepsilon<0$ according to the rule

$$\Phi(\varepsilon)=\Phi(2u_1+\varepsilon) \ . \qquad (A15)$$

As the boundary condition at $x=0$ we use the condition for the energy distribution of the electron flux density to be equal to a given function $j_f(u)$.

This boundary condition can be written as

$$\frac{1}{3}\left[\frac{2e}{m}\right]^{1/2}uf_1(u,0)=j_f(u) \qquad (A16)$$

or

$$-\frac{1}{3}\left[\frac{2e}{m}\right]^{1/2}\frac{E}{N}\frac{u}{q_t}\frac{\partial f_0(u,0)}{\partial w}=j_f(u) \ . \qquad (A17)$$

We represent the function $j_f(u)$ as

$$j_f(u)=\frac{1}{3}\left[\frac{2e}{m}\right]^{1/2}\frac{E}{N}\frac{u}{q_t}\psi(u) \ . \qquad (A18)$$

Equations (A17) and (A18) result in the following expression for the function $\Phi(\varepsilon)$:

$$\Phi(\varepsilon)=-\frac{\psi(\varepsilon)}{\phi'(\varepsilon)}-B_2 \quad \text{for } \varepsilon>u_1 \ , \qquad (A19)$$

$$\Phi(\varepsilon)=-\frac{q_t(u_1)}{u_1\phi'(u_1)}\left[\frac{\psi(\varepsilon+u_1)}{\phi'(\varepsilon+u_1)}I(\varepsilon+u_1)+\frac{\varepsilon}{q_t(\varepsilon)}\psi(\varepsilon)\right]$$
$$\text{for } 0\le\varepsilon<u_1 \ . \qquad (A20)$$

For $\varepsilon<0$ the function Φ is defined by Eq. (A15). The continuity of f_0 with respect to the variable ε is obtained by setting

$$B_2=-\psi(2u_1)/\phi'(2u_1)$$
$$+2q_t(u_1)\psi(2u_1)/q_t(2u_1)\varphi'(u_1) \ . \qquad (A21)$$

In our particular calculations, we have used as the function $j_f(u)$ the energy distribution of the electron flux density corresponding to the function f_0 in the uniform positive column. This function is given by Eqs. (A7)–(A9) with $C_1(\varepsilon)=0$, $C_0(\varepsilon)=C_2(\varepsilon)=$const$=B_0$, and $E=E_0$, where E_0 is the electric field far away from the orifice. In that case

$$\psi(u)=-\frac{E_0}{E}B_0\phi_0'(u) \quad \text{for } u\ge u_1 \ ,$$
$$\qquad\qquad\qquad\qquad\qquad\qquad (A22)$$
$$\psi(u)=\frac{E_0}{E}\frac{q_t(u)}{u}I_0(u+u_1)B_0 \quad \text{for } u<u_1 \ ,$$

where the functions $\phi_0(u)$ and $I_0(u)$ have the same meaning as the functions $\phi(u)$ and $I(u)$, but for $E = E_0$. Calculations have been performed with the momentum-transfer cross section in neon approximated by the empirical formula

$$q_t(u) = 5.35u^{1/3}/[1+(u/40)^{1.4}] \ . \tag{A23}$$

As the total inelastic cross section of mercury q^* we have used the value derived from the literature data and our modeling of the uniform positive-column plasma. The function $q^*(u)$ is shown in Fig. 14. The functions $\phi(u)$ and $\phi_0(u)$ have been obtained by numerical solution of Eq. (A6).

2. The region beyond the orifice

The equations for the functions f_0 and f_1 in this region can be obtained from Eqs. (A2) by setting $E = 0$.

Considering again the condition (A5), one can obtain the general expression for the function f_0 in the following forms. For $u < u_1$,

$$f_0(u,x) = A_2(u)\exp[-y/a(u)] \ . \tag{A24}$$

For $u > u_1$,

$$\begin{aligned}
f_0(u,x) = &-A_1(u)y + A_2(u+u_1)F_q(u) \\
&\times \{1-\exp[-a(u+u_1)y]\} \\
&+ A_0(u) \ .
\end{aligned} \tag{A25}$$

Here y is the distance from the orifice, and

$$\begin{aligned}
a(u) &= [3NN_{Hq}q^*(u)q_t(u)]^{1/2} \ , \\
F_q &= \frac{q_t(u)(u+u_1)}{q_t(u+u_1)u} \ .
\end{aligned} \tag{A26}$$

Functions $A_0(u)$, $A_1(u)$, $A_2(u)$ are arbitrary functions of the electron kinetic energy.

The function $f_1(u,x)$ is equal to

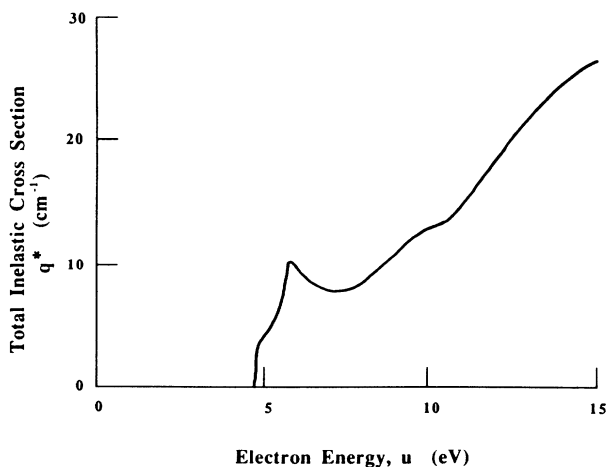FIG. 14. Total inelastic cross section of Hg, q^* in cm^{-1}.

$$f_1(u,x) = -\frac{1}{Nq_t}\frac{\partial f_0}{\partial x} \ . \tag{A27}$$

Calculation of the electron flux density results in the expression

$$j = \frac{1}{3N}\left[\frac{2e}{m}\right]^{1/2}\int_0^{u_1}\frac{u}{q_t}A_1(u)du \ , \tag{A28}$$

which does not depend on x. Thus the condition of the flux conservation is always satisfied. As the boundary condition at the orifice $(y=0)$, we use again the condition (A16) for the distribution of the electron flux density which takes the form

$$\frac{1}{3}\left[\frac{2e}{m}\right]^{1/2}uf_1(u,0) = j_f(u) \ , \tag{A29}$$

where $f_1(u,0)$ is given by Eqs. (A24)–(A27). The function $j_f(u)$ has to be taken now as

$$j_f(u) = -\frac{1}{3}\left[\frac{2e}{m}\right]^{1/2}\frac{E}{N}\frac{u}{q_t}\frac{\partial f_0(u,d)}{\partial w} \ , \tag{A30}$$

where $\partial f_0/\partial w$ has to be calculated using the expression for f_0 in the region in front of the orifice. This results in the expressions

$$A_2(u) = -E[\Phi(\varepsilon_d)+B_2]\phi'(u)/a(u) \ , \tag{A31}$$

$$A_1(u) = -E\frac{u_1\phi'(u_1)}{q_t(u_1)}[\Phi(\varepsilon_d)+\Phi(\varepsilon_d+u_1)+B_2]\frac{q_t(u)}{u} \ ,$$

where $\varepsilon_d = u - Ed$.

The function f_0 cannot be made continuous at $u = u_1$ for any value of x. This is due to the fact that effects of electron-electron interaction or nonzero electric field have not been considered. In that case there is no mechanism which can transfer electrons from the energy domain $u < u_1$ to the energy domain $u > u_1$, and the distribution function for $u > u_1$ changes independently of the distribution function for $u < u_1$.

In this situation, the function $A_0(u)$ can be determined by requiring f_0 to be positive in the quasiequipotential region beyond the orifice. That gives

$$A_0(u) = A_1(u)y_m \ , \tag{A32}$$

where y_m is the length of the quasiequipotential region.

The function f_0 which we have obtained diverges to infinity at $u \to 0$. This is due to the fact that the energy-dependent electron diffusion coefficient goes to zero as

$$\sqrt{u}/q_t(u) \to 0 \ .$$

This results in the unrestricted accumulation of electrons at $u \to 0$. Actually, if the diffusion term in the kinetic equation goes to zero, then electron-electron interaction will take over for small enough energies and restrict the accumulation. We have made a rough estimate of energy u_0 at which the electron interaction term becomes equal to the diffusion term.

This has to give u_0 (in volts)

$$u_0 \simeq (0.6 \times 10^{-12} N_e p y_m^2)^{6/7} , \qquad \text{(A33)}$$

where N_e is the electron number density in cm^{-3} and p is the pressure in torr, and y_m is expressed in cm. Accordingly, the singularity in the EEDF has been regularized by assuming $f_0(u) = f(u_0)$ for $u < u_0$.

Note, this procedure has been applied only for plotting the EEDF. All calculations of the electron number density, average energy, etc. have been performed before the regularization. The regularization practically does not change any calculational values.

[1]R. Lagushenko, R. Pai, and J. Maya, U.S. Patent No. 4,736,134; J. Maya and R. Lagushenko, U.S. Patent pending; R. Lagushenko and J. Maya, U.S. Patent pending.

[2]I. Langmuir, Phys. Rev. 33, 954 (1929).

[3]Y. S. Levine and F. W. Crawford, J. Plasma Phys. 23, 223 (1980).

[4]N. Sato, in Proceedings of the Symposium on Plasma Double Layers, Roskilde, 1982 (unpublished).

[5]N. Hershkowitz, Space Sci. Rev. 41, 351 (1985).

[6]D. Anderson, J. Phys. D 10, 1549 (1977).

[7]V. Godyak, R. Lagushenko, and J. Maya, Bull. Am. Phys. Soc. 32, 1146 (1987).

[8]R. Lagushenko, V. Godyak, and J. Maya, Bull. Am. Phys. Soc. 33, 126 (1988).

[9]B. N. Ganguly and A. Garscadden, Bull. Am. Phys. Soc. 32, 1165 (1987).

[10]J. D. Swift and M. J. R. Schwar, Electric Probes for Plasma Diagnostics (Iliffe, London, 1971).

[11]W. Verweij, Philips Res. Rep. Suppl. 2, 1 (1961).

[12]J. F. Waymouth, J. Appl. Phys. 30, 1904 (1959).

[13]K. F. Schoenberg, Rev. Sci. Instrum. 49, 1377 (1978).

[14]V. A. Godyak, Bull. Am. Phys. Soc. 31, 197 (1986).

[15]R. L. E. Boyd and N. D. Twiddy, Proc. R. Soc. London, Ser. A 250, 53 (1950).

[16]J. F. Waymouth, Electric Discharge Lamps (MIT, Cambridge, MA, (1971), p. 83.

[17]Y. Tzeng and E. E. Kunhardt, Bull. Am. Phys. Soc. 28, 180 (1983).

[18]P. Segur, M. Yousfi, J. P. Bouef, E. Marode, A. J. Davies, and J. G. Evans, in Electrical Breakdown and Discharges in Gases, edited by E. E. Kunhardt and L. H. Luessen (Plenum, New York, 1981), p. 331.

[19]T. N. An, E. Marode, and P. C. Johnson, J. Phys. D 10, 2317 (1977).

[20]L. E. Kline, J. Appl. Phys. 58, 3175 (1985).

[21]J. P. Bouef and E. Marode, J. Phys. D 15, 2169 (1982).

[22]N. Sato and H. Tagashira, J. Phys. D 18, 2451 (1985).

[23]T. J. Moratz, L. C. Pitchford, and J. N. Bardsley, J. Appl. Phys. 61, 2146 (1987).